



# Sulfur/Nitrogen Co-Doped In-Plane Porous Carbon Nanosheets as Superior Anode of Potassium-Ion Batteries

Guilan Li,<sup>[a]</sup> Anding Xu,<sup>[a]</sup> Fulan Zhong,<sup>[b]</sup> Chuyun Huang,<sup>[a]</sup> Hao Sun,<sup>[b]</sup> Zhiguang Xu,<sup>[c]</sup> Songping Wu,<sup>\*[b, d]</sup> and Yurong Yan<sup>\*[a, e]</sup>

Carbonaceous materials are regarded as prospective anode candidates of potassium-ion batteries. However, the rate capability and cycling stability of classic carbon materials are still far from satisfactory. Herein, we exploit a facile and low-cost strategy to enable the precise synthesis of sulfur/nitrogen co-doped in-plane porous carbon nanosheets with fishnet-shaped microstructure (SN-CNSs). The well-designed in-plane porous structure and the interconnected carbon flake network can accelerate the diffusion of potassium ions, alleviate volume

expansion, and provide sufficient active sites. As a result, the SN-CNSs deliver an impressively reversible capacity of  $248 \text{ mAh g}^{-1}$  at a current density of  $1 \text{ A g}^{-1}$  after 4500 cycles, and an excellent rate capacity of  $137.3 \text{ mAh g}^{-1}$  after 4000 cycles under  $5 \text{ A g}^{-1}$ . Density functional theory (DFT) calculations further verify the advantage of S/N co-doping in the adsorption/diffusion of K-ion in SN-CNSs materials. Such an excellent performance shows that SN-CNSs possess a great potential to be a superior anode of potassium-ion batteries.

## Introduction

The exhausting resource and the rising cost of lithium have become an insurmountable bottleneck for sustainable development of lithium-ion batteries (LIBs). Therefore, the exploitation of new-concept batteries has been evolving into a highly concern problem.<sup>[1]</sup> So far, potassium-ion batteries (PIBs) are attracting tremendous attention as promising alternatives for LIBs due to their merits of massive resources, low price, eco-friendliness, as well as low redox voltage ( $-2.93 \text{ V}$  vs. standard hydrogen electrode).<sup>[2,3]</sup> However, the PIBs must face and overcome their unique challenges, e.g.,  $1.38 \text{ \AA}$  radius of potassium ion, which resulted in severe volumetric expansion and sluggish kinetics in the process of getting in and out of its host.<sup>[4]</sup>

Therefore, it is crucial to identify suitable anode materials for efficiently accommodating  $\text{K}^+$  upon depotassiation/potassiation.<sup>[5–7]</sup> Up to now, several researches highlight alloy-typed materials,<sup>[8–10]</sup> conversion-typed materials,<sup>[11–14]</sup> and intercalation-typed materials.<sup>[3,15,16]</sup> Among all the categories, carbon was used as a prospective candidate of anode in consideration of its vast source, stable physical/chemical properties, excellent operability, high conductivity, and environmental benignity.<sup>[3]</sup> However, the rate capability and the cycling stability of classic carbon materials still maintained a great challenge for practical application due to the severe pulverization.<sup>[17]</sup>

To conquer the above obstacles, the introduction of heteroatoms into carbon has been considered as an effective strategy, in general, can change the distribution of electron cloud in micro-region and further optimize the dynamics of short-range electron transport. Huang et al. reported N-doped 3D mesoporous carbon nanosheets obtained a reversible capacity of  $321 \text{ mAh g}^{-1}$  at  $5 \text{ A g}^{-1}$ , and a rate performance of  $161 \text{ mAh g}^{-1}$  at  $20 \text{ A g}^{-1}$  for PIBs.<sup>[18]</sup> In our previous work,<sup>[19]</sup> N-doped CNFs delivered an impressively reversible capacity of  $351.1 \text{ mAh g}^{-1}$  after 500 cycles at a current density of  $200 \text{ mA g}^{-1}$ . Even at a high rate of  $5 \text{ A g}^{-1}$ , reversible capacity of  $122.3 \text{ mAh g}^{-1}$  has been enduringly retained after 20,000 cycles. Considering the synergistic effect between different heteroatoms, the introduction of dual heteroatoms in carbon materials played an important role in increasing the reactive sites, expanding interlayer spacing, and enhancing wetting properties, further leading to accelerated dynamics, improved potassium storage, and superior cyclability.<sup>[6]</sup> Sulfur/oxygen co-doped porous hard carbon microspheres have been yielded, enabling a potassiation capacity of  $226.6 \text{ mAh g}^{-1}$  at  $50 \text{ mA g}^{-1}$  after 100 cycles and  $108.4 \text{ mAh g}^{-1}$  at  $1.0 \text{ A g}^{-1}$  after 2000 cycles.<sup>[20]</sup> Unfortunately, on the one hand, the above materials commonly requested complicated preparation procedures, making them too tedious to meet practical demands for

[a] G. Li, Dr. A. Xu, C. Huang, Prof. Y. Yan  
School of Materials Science and Engineering  
South China University of Technology  
Guangzhou 510641, China  
E-mail: yryan@scut.edu.cn

[b] F. Zhong, H. Sun, Prof. S. Wu  
School of Chemistry and Chemical Engineering  
South China University of Technology  
Guangzhou 510641, China  
E-mail: chwsp@scut.edu.cn

[c] Prof. Z. Xu  
Key Laboratory of Theoretical Chemistry of Environment  
Ministry of Education, School of Chemistry  
South China Normal University  
Guangzhou 510006, China

[d] Prof. S. Wu  
Guangdong Key Laboratory of Fuel Cell Technology  
Guangzhou 510641, China

[e] Prof. Y. Yan  
Key Lab of Guangdong High Property & Functional Polymer Materials  
Guangzhou 510640, China

Supporting information for this article is available on the WWW under <https://doi.org/10.1002/batt.202100379>

PIBs. On the other hand, for an energy-storage device, stable energy output is very important. Therefore, the long and stable platforms of potassiation/depotassiation are a key indicator of anode materials. However, highly-disordered crystal structure of hard carbon, instead of graphite, should inevitably produce more surface-adsorbed route, rather than diffusion-controlled path. In this circumstance, the clear platforms of potassiation/depotassiation ceased to occur, leading to the fluctuation of energy output. Therefore, how to integrate the merit of layered graphitized carbon and highly disordered hard carbon become urgent importance to answer this seemingly paradoxical problem, i.e., high-rate and long-life of carbon materials.

Herein, we exploited a facile and low-cost strategy to the precise synthesis of sulfur/nitrogen co-doped carbon nanosheets (SN-CNSs) with uniformly in-plane nano-holes, acting as a reliable anode of PIBs. A hierarchical porous structure has been delicately generated by a multi-scaled templates method. Importantly, the catalysis of transition metals (i.e., iron) tended to trigger a low temperature graphitization of carbon lattices surrounding them, and finally forming carbon nanosheets with uniformly distributed nanoholes in their plane after moving iron nanoparticles away. As a result, SN-CNSs rendered a high potassiation capacity of  $248 \text{ mAhg}^{-1}$  at a current density of  $1 \text{ Ag}^{-1}$  after 4500 cycles. Density functional theory (DFT) calculations further verified the advantage of S/N co-doping in the adsorption/diffusion of K-ion in the porous carbon material.

## Results and Discussion

The schematic illustration of the preparation of SN-CNSs was depicted in Figure 1(a). Here, hierarchically-templated method followed by low temperature catalysis was adopted to generate partially graphitized in-plane porous carbon nanosheets, possessing evenly-distributed in-plane fishnet-shaped nanoholes. Iron acetylacetone acted as both carbon resource and iron resource of monatomic catalysts as well as nano-scaled template. Sodium chloride crystal played dual roles as a micro-sized template and a ball milling agent enhancing rolling iron acetylacetone powders to make the flakes. The subsequent added sulfur powder and urea, as sulfur resource and nitrogen resource, respectively, were evenly mixed with aforementioned powders to form precursor. After pyrolysis and thermal reduction process, NaCl crystals remained unchanged and the iron acetylacetone was successfully transformed into 3D carbon network, into which in-situ synthesized iron nanoparticles via carbothermal reduction were mono-dispersedly buried. Utilizing catalysis of fresh iron atoms at high temperature, the lattices of hard carbon surrounding iron were gradually ordered to generate graphitized carbon.<sup>[21]</sup> After washing off the iron nano-particles and NaCl, sulfur/nitrogen co-doped carbon nanosheets with in-plane nanoholes were produced, abbreviated as SN-CNSs.

In SEM image of SN-CNSs (Figure 1b), interconnected 3D carbon network has been perceived to be supported by carbon walls. Among them, micro-sized holes could be considered as the consequence of removing NaCl templates (red dotted

circle). In comparison with the sample no ball milling, it was believed that ball milling step was critical to the formation of the topography during the synthesis process (Figure S1).

TEM image showed transparent fishnet-shaped microstructures in carbon plane, accompanying with ridges of carbon wall of 5–10 nm thickness (blue arrows) and rings (brown arrows) (Figure 1c). Of special note is the plenty of uniform nanopores of ~8 nm, as the result of expelling iron nano-particles from their previous locations, presented themselves in almost all region of plane, producing in-plane porously-structured carbon (Figure 1d and e). Average lattice spacing of 0.391 nm could be examined to occur in the ring-like border of nanopores because of low-temperature graphitization catalyzed by iron atom via in-situ reduction (Figure S2).<sup>[22]</sup> The fishnet-shaped carbon could be discerned to be comprised of 2–4 layers with slightly improved layer spacing, reasonably originated from low crystalline degree and heteroatom doping. The diffraction ring of SAED pattern could be distinguished, corresponding to characteristic planes of (002) for graphite (inset in Figure 1d). Above fact robustly affirmed the presence of graphitized carbon in short-range region. The contour of the intertwining distribution of elements in carbon meant that sulfur and nitrogen were evenly dispersed on the 3D skeleton, in avoidance of obvious agglomeration and segregation (Figure 1f–j). Similar approach was also accepted to yield the S-CNSs, N-CNSs, and CNSs with analogously-structured features for comparing (Figure S3a–c).

Here, XRD analysis was utilized to get further insight into the phase component for as-synthesized carbon. Firstly, there appeared a strong diffraction peak in the carbon derived from the thermal decomposition products of iron acetylacetone without milling, being assigned to the (002) plane of graphite, meaning a remarkable ordered structure of aggregated carbon (Figures 2a and S3d–f). However, the characteristic diffraction peaks appeared to become broader at  $23^\circ$ – $25^\circ$  for milled samples, alluding the emergence of disordered carbon originated from flaky carbon precursor using milling method. The obvious peak down-shift of (002) plane to  $23.43^\circ$  was strongly indicative of an enlarged interlayer spacing in SN-CNSs compared with those of S-CNSs ( $23.86^\circ$ ), N-CNSs ( $23.66^\circ$ ) and CNSs ( $24.17^\circ$ ).<sup>[23]</sup> The significantly enhanced D-peak of SN-CNSs in Raman spectroscopes indicated that most defects and highly disordered structures have emerged in SN-CNSs as compared with the no milling (Figures 2b and S4).<sup>[24]</sup> The specific surface area and porous texture were characterized using  $\text{N}_2$ -adsorption method. The isotherm curves of SN-CNSs and control samples were gathered with a type IV isotherm, pointing to the characteristic of mesoporous materials with specific surface area of  $261.68 \text{ m}^2 \text{ g}^{-1}$ , which further ensured the hierarchical microstructures with pore diameter of both 3–15 nm and 24 nm (Figure S5).<sup>[25]</sup> However, the measurement range of  $\text{N}_2$  adsorption is limited to the pore size of 1.7–300 nm. To characterize the nano-pores size less than 2 nm,  $\text{CO}_2$  was used as a probe gas to obtain more accurate information on atomic level. Figure 2(c and d) showed the  $\text{CO}_2$  adsorption isotherm of the SN-CNSs, with a specific surface area of  $200.08 \text{ m}^2 \text{ g}^{-1}$ . The pore volume is  $0.5517 \text{ cm}^3 \text{ g}^{-1}$ , mainly contributed by the pores

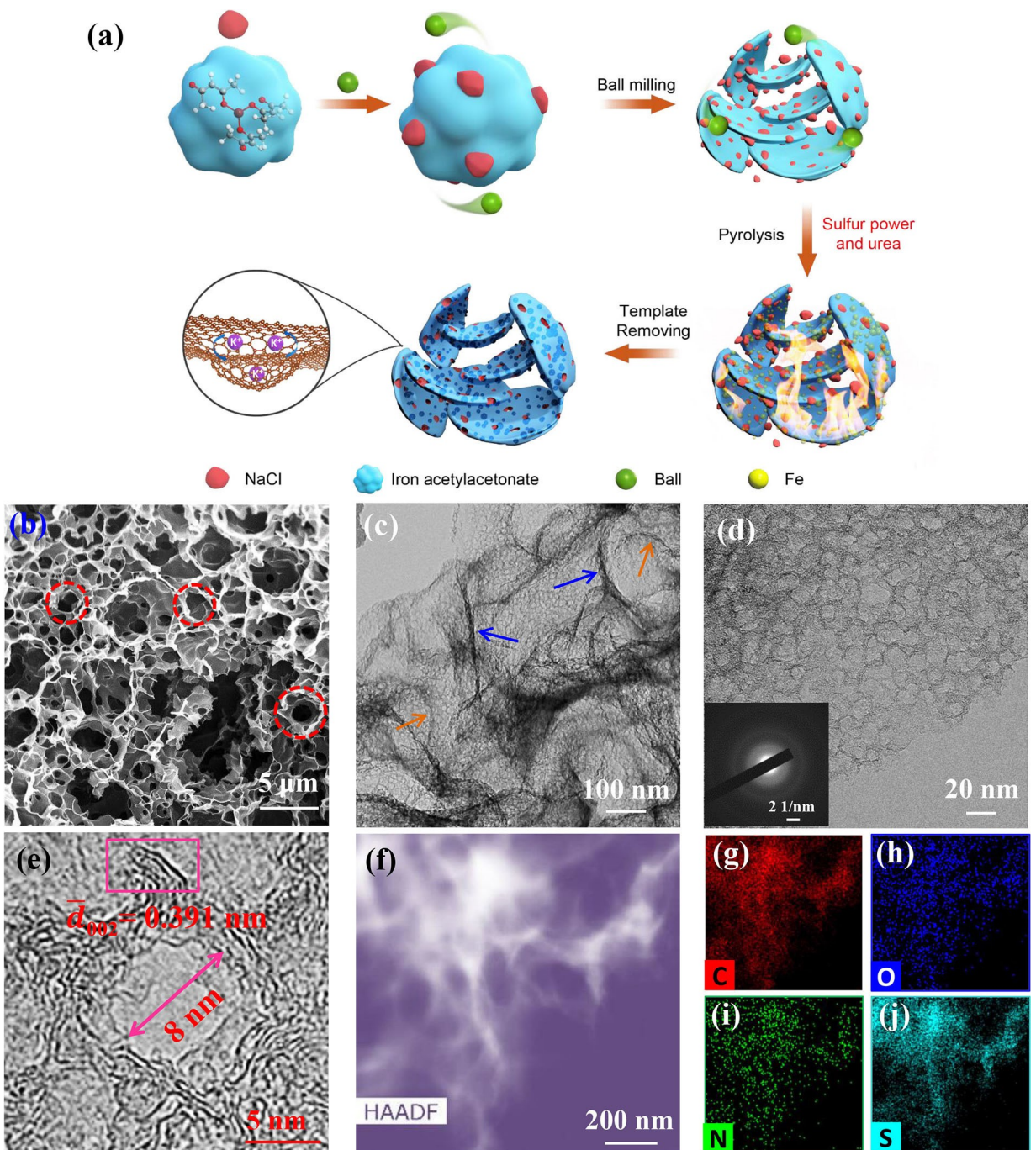


**Figure 1.** a) Schematic illustration of the preparation of SN-CNSs. b) SEM image of SN-CNSs. c, d) TEM images of SN-CNSs (inset: SAED pattern). e) HRTEM image and f-j) element mappings of C, O, N and S for SN-CNSs.

with a width between 0.4 and 0.8 nm. Such a multi-scaled pore structure would produce more sites for energy storage, and further improve reversible capacity when using them as potassium-storage materials.<sup>[26]</sup>

In the X-ray photoelectron spectroscope (XPS) spectrum, four distinct peaks of C 1s, N 1s, O 1s and S 2p, located at 284.8, 400.8, 300.0, 531.8 and 163.8 eV, respectively, have been successfully detected in SN-CNSs (Figure S6a). The high-resolution C 1s peak could be deconvoluted into four peaks at 284.8, 285.8, 287.0 and 290.4 eV (Figure S6b), indexing to

graphitic carbon ( $\text{sp}^2$  hybridized) C–C bond, C–N/C–O bond, C–S bond, and C=O bond, respectively.<sup>[27–29]</sup> More notably, N 1s spectrum of SN-CNSs was composed of pyridinic-N (11.08% N-6), pyrrolic-N (73.98% N-5) and graphitic-N (14.94% N-Q), located at 398.6, 401.2 and 402.5 eV (Figure 2e), respectively.<sup>[30]</sup> In the high-resolution S 2p spectrum, two sharp peaks could be found to arise at 163.7 and 164.9 eV, ascribed to the S 2p<sub>3/2</sub> and S 2p<sub>1/2</sub> peaks of the –C–S–C– covalent bonds (Figure 2f), respectively. Accompanying with them is a weak peak centered at the 168.4 eV, concerning to oxidized sulfur species

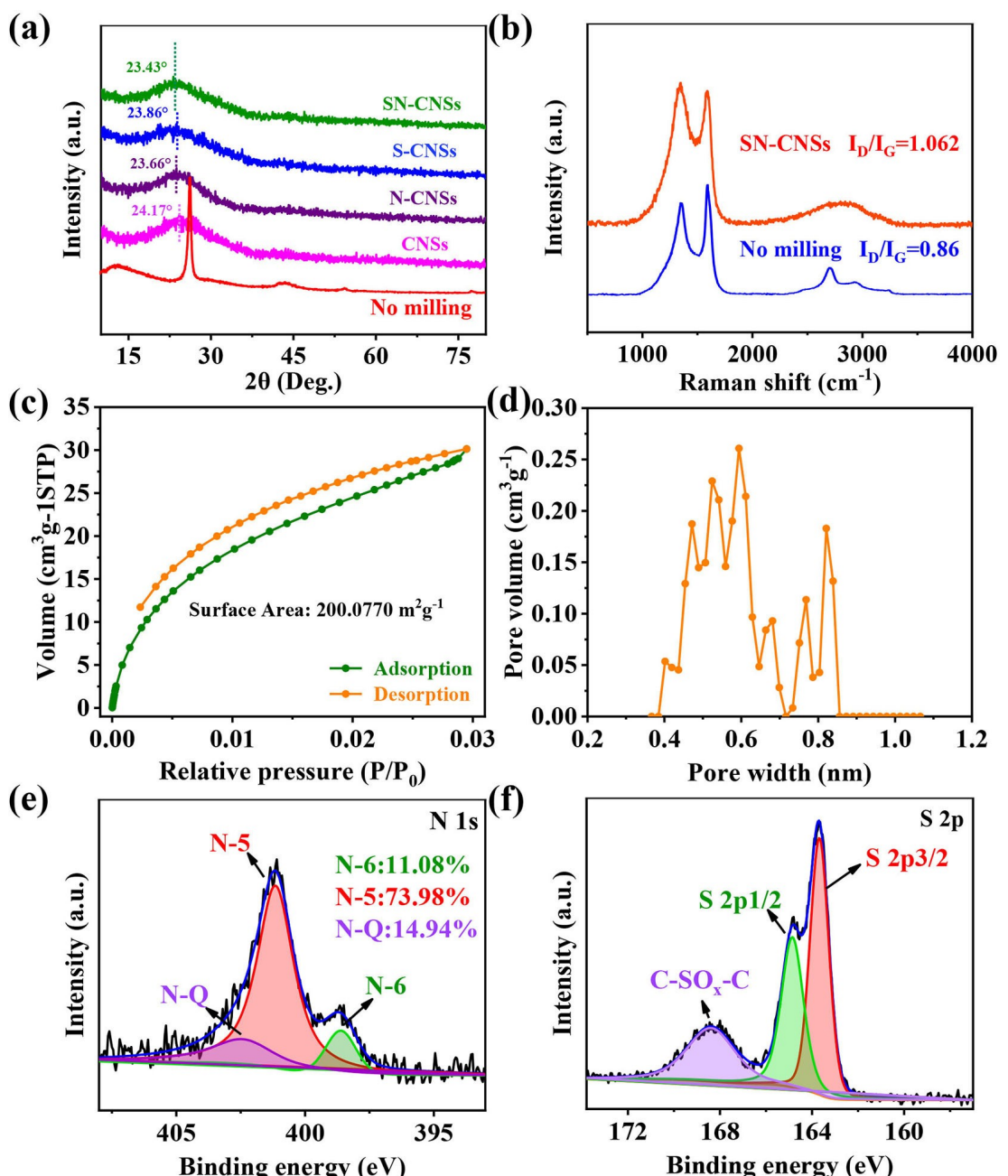


**Figure 2.** Structure characterizations. a) XRD patterns of SN-CNSs, S-CNSs, N-CNSs, CNSs and the thermal decomposition products of iron acetylacetone without milling, respectively. b) Raman spectra. c)  $\text{CO}_2$  adsorption-desorption isotherm and d) pore size distribution of SN-CNSs. e) N 1s and f) S 2p XPS spectra of SN-CNSs.

( $\text{C}-\text{SO}_x-\text{C}$ ).<sup>[31]</sup> Above facts indicated that sulfur and nitrogen heteroatoms have been effectively incorporated into the hierarchical porous carbon framework of SN-CNSs, giving rise in the changes of the density of electron cloud and lattice parameters of carbon materials.

Considering all above, we strongly believed that SN-CNSs have been rationally designed and synthesized. Such carbon nanosheets possessed a remarkable in-plane porous feature, like a fishnet, tending to decrease diffusion distance and facilitate rapid transportation of  $\text{K}^+$  ions, which were the utterly noticed issues in following works.

K-storage behavior of SN-CNSs electrode was firstly assessed using cyclic voltammetry (CV) within a potential window of 0.01–3.0 V (vs.  $\text{K}^+/\text{K}$ ) at a scan rate of  $0.1 \text{ mVs}^{-1}$ . As depicted in Figure 3(a), two strong peaks centered at  $\sim 0.56$  and  $\sim 0.11$  V appeared in the first cathodic scanning and tended to vanish in the following cycles, which could be ascribed to the decomposition of electrolyte and formation of solid-electrolyte interface (SEI) layer.<sup>[32]</sup> In subsequent scanning, a redox couple appeared at 0.86/1.67 eV, originating from the reaction between sulfur and potassium ( $2 \text{ K} + \text{S} \leftrightarrow \text{K}_2\text{S}$ ).<sup>[33,34]</sup> Subsequently, the following cathode peak at 0.01 V corre-

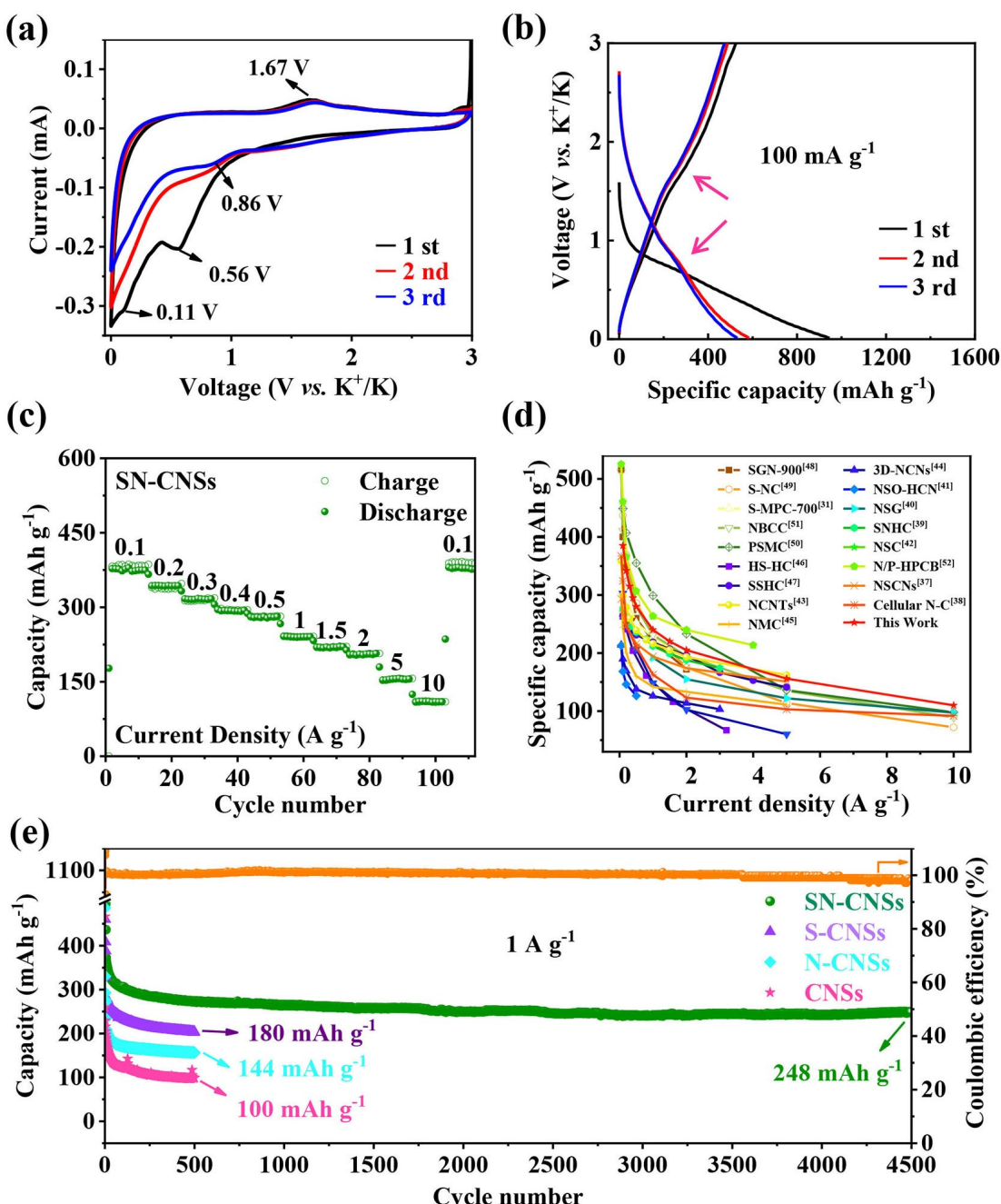


**Figure 3.** a) CV curves of SN-CNSs electrode at a scan rate of  $0.1 \text{ mV s}^{-1}$ . b) Galvanostatic charge/discharge profiles at  $100 \text{ mA g}^{-1}$  of SN-CNSs. c) Rate capability of SN-CNSs. d) Rate capabilities of SN-CNSs compared with those of carbonaceous anode materials for PIBs reported in the literatures. e) Long-term cycling performances of SN-CNSs and control samples at  $1 \text{ A g}^{-1}$  after activation for five cycles at  $0.1 \text{ A g}^{-1}$ .

sponded to the insertion of potassium ions to form a compound of  $\text{KC}_8$ . Correspondingly, the wide anodic peak centered at 0.3 V could be derived from the extraction of K-ion. Some analogous features were also proven by galvanostatic charge-discharge profiles, where initial charge/discharge capacities of  $524.8$  and  $946.4 \text{ mAh g}^{-1}$  have been provided at a current density of  $100 \text{ mA g}^{-1}$  (Figure 3b), with an initial coulombic efficiency (ICE) of  $55.5\%$  which was ascribed to high specific surface area and surface defects, causing ion traps and forming more SEI film in the initial cycle. The low ICE could be

addressed by the pre-potassiation, adjustment of defect concentration,<sup>[35]</sup> and binder optimization.<sup>[36]</sup> After the initial cycle, the profiles highly overlapped and displayed a redox platform (red arrows), greatly raising the potential platform of potassium intercalation and effectively avoiding the risk of potassium dendrite. After 250 cycles, SN-CNSs electrode delivered a reversible capacity of  $258.2 \text{ mAh g}^{-1}$  at  $0.5 \text{ A g}^{-1}$ , with no obvious capacity loss from 50th cycle, implying the good reversibility of such a doped carbon (Figure S7). SN-CNSs electrode afforded excellent rate performances, i.e., reversible

capacities of 385, 342, 315, 295, 280, 240, 220, 205, 156 and 110 mAh g<sup>-1</sup> at current densities of 0.1, 0.2, 0.3, 0.4, 0.5, 1.0, 1.5, 2.0, 5.0 and 10.0 Ag<sup>-1</sup> (Figure 3c), respectively. When the current density was back to 0.1 Ag<sup>-1</sup>, the electrode remained a high capacity of 381 mAh g<sup>-1</sup>, ensuring a robust capability in answering current shock for such a doped carbon. As a contrast, S-CNSs, N-CNSs and CNSs electrodes rendered rather poor rate capabilities of 365, 150 and 132 mAh g<sup>-1</sup> when the current density recovered to 0.1 Ag<sup>-1</sup> (Figures S8–S10), respectively. More importantly, such a shocking rate performance of SN-CNSs is superior to most of the reported carbonaceous anodes for PIBs (Figure 3d, Table S1), reflecting the most notable capability in driving highly-powered devices for SN-CNSs electrode to date.<sup>[31,37–52]</sup>

Following above research, the long-term cycling performance has excited our ever-growing interest. Due to the clear potential for SN-CNSs electrode at high current density, the question is if an outstanding durability could be realized. SN-CNSs electrode rendered a satisfactory reversible capacity of 248 mAh g<sup>-1</sup> at 1 Ag<sup>-1</sup> after 4500 cycles, with a high coulombic efficiency of nearly 100% (Figure 3e). Such a remarkable performance, catching the eyes of researchers, could be confirmed with a series of experimental data, e.g., 180.1 mAh g<sup>-1</sup> at 2 Ag<sup>-1</sup> after 1630 cycles and 137.3 mAh g<sup>-1</sup> even at high-rate of 5 Ag<sup>-1</sup> after 4500 cycles (Figure S11). By contrast, the electrochemical performance of S-CNSs, N-CNSs and CNSs electrodes were measured to gather poor capacities of 180, 144, and 100 mAh g<sup>-1</sup> at 1 Ag<sup>-1</sup> for 500 cycles, respectively. It was worth noting that high cycling stability was achieved when SN-CNSs were served as anode assembled in full cell with a Prussian blue cathode (Figure S12).

To elucidate deep roots of greatly enhanced performance, EIS patterns, pseudo-capacitance contribution and galvanostatic intermittent titration (GITT) technique have been performed to observe more explicit kinetics features of SN-CNSs electrodes. Electrochemical impedance spectroscopy test was performed to characterize the resistance of the samples after 500 cycles at 0.5 Ag<sup>-1</sup> (Figure 4a). Merged  $R_{ct+SEI}$  of SN-CNSs could be simulated as 609 Ω, far lower than those of its counterparts (Figure S13 and Table S2), being indicative of the lower charge-transfer resistances and faster K<sup>+</sup> diffusion kinetics in SN-CNSs electrode.

After running 20 cycles to exclude possible impact of irreversible reaction, the electrode was operated under various scan rates, from 0.3 to 1.5 mV s<sup>-1</sup>, to get their cyclic voltammetry (CV) curves for calculating its pseudo-capacitance (Figure 4b). As scan rate increased, the (de)potassiation peaks of SN-CNSs electrode became slightly broader and kept their original shapes. The relationship between the peak current ( $i_p$ ) and the scan rate ( $v$ ) was in harmony with a power law, according to  $i_p = av^b$ , where  $i_p$  represents peak current,  $v$  means scan rate, and  $a$  or  $b$  are adjustable constants.<sup>[53]</sup> For the current carbon electrode, well-defined linear slopes have been fitted to get an average  $b$  value of 0.87 (Figure 4c), suggesting the dominated capacitive behavior for K<sup>+</sup> storage.<sup>[54]</sup> The capacitive charge contribution could be further distinguished according to the equation of  $i = k_1 v + k_2 v^{1/2}$ . The current response  $i$  at a

fixed potential could be regarded as the combination of surface-controlled and diffusion-dependent processes, which are proportional to  $v$  and  $v^{1/2}$ . By counting  $k_1$  and  $k_2$  at fixed potentials, the proportion of the current from each contribution might be quantified into the two processes. The profiles of the current contributed by the capacitive process was illustrated in orange shadow region, as 55% at a scan rate of 0.3 mV s<sup>-1</sup>, together with the total current response (Figures 4d and S14). The capacitive fraction increased with scan rates increasing, gradually reaching 74% at 1.5 mV s<sup>-1</sup> (Figure 4e).

GITT measurement was utilized to assess the diffusion coefficients ( $D_k$ ) of potassium in SN-CNSs electrode and control sample of CNSs electrode by applying a series of current pulses at 0.5 Ag<sup>-1</sup> for 2 min followed by a 10 min relaxation process (Figures 4f and S15). The function was introduced to calculate the value of  $D_k$  based on Equation (1):<sup>[55]</sup>

$$D = \frac{4}{\pi \tau} \left( \frac{n_m V_m}{S} \right)^2 \left( \frac{\Delta E_s}{\Delta E_t} \right)^2 \left( \tau \ll \frac{L^2}{D} \right) \quad (1)$$

where  $\tau$  is the duration of the current impulse,  $n_m$  is the number of moles,  $V_m$  is the molar volume of the active materials,  $S$  represents the geometric area of the electrode,  $\Delta E_s$  is the equilibrium potential difference between before and after the current pulse, and  $\Delta E_t$  means the potential difference during the current pulse. The results exhibited that the potassium-diffusion coefficient of SN-CNSs was higher than that of CNSs upon potassiation/depotassiation, such as average  $3 \times 10^{-7}$  cm<sup>2</sup> s<sup>-1</sup> for potassiation (Figure 4g and h). The faster kinetics of SN-CNSs might be contributed from the favorable potassium ion diffusion property after experiencing sulfur/nitrogen co-doping.

Microstructure evolution has given a deep insight into their long-life and high-rate of carbon electrode (Figure 5a and b). The morphology of carbon sample, harvested from electrode after 1000 cycles at 1 Ag<sup>-1</sup>, was carefully observed with TEM images (Figure S16). In fully-charged state, the carbon nanosheets with nano-holes refused to be damaged, and the original structure could be perfectly maintained even after deep cycling.

Ex-situ Raman spectra of S/N co-doped carbon nanosheets electrode after two cycles, were implemented to form an essentially molecular-levelled opinion of storing potassium ions (Figure 5c and d). In discharged-state, with the potential decreasing, there emerged the blue-shifted G peak, from the initial state (1590 cm<sup>-1</sup>) to fully potassiated state (1599 cm<sup>-1</sup> at 0.01 V), because carbon tended to accept more electrons to balance the insertion of K<sup>+</sup> ions.<sup>[56]</sup> Subsequently, obviously red-shifted G peaks were detected as the result of driving potassium out of carbon during charging. Therefore, ex-situ Raman spectra have perfectly corroborated the reversible process on the potassium shuttling through carbon host.

Ex-situ XRD patterns of carbon, taken from electrode in the first cycles, have appealed our great concern. After being discharged to 1.0 V, an explicitly observable diffraction peak emerged at ~22.0°, revealing the formation of KC<sub>36</sub> (Figure 5e). Upon further potassiation, strength of KC<sub>36</sub> diffraction peaks

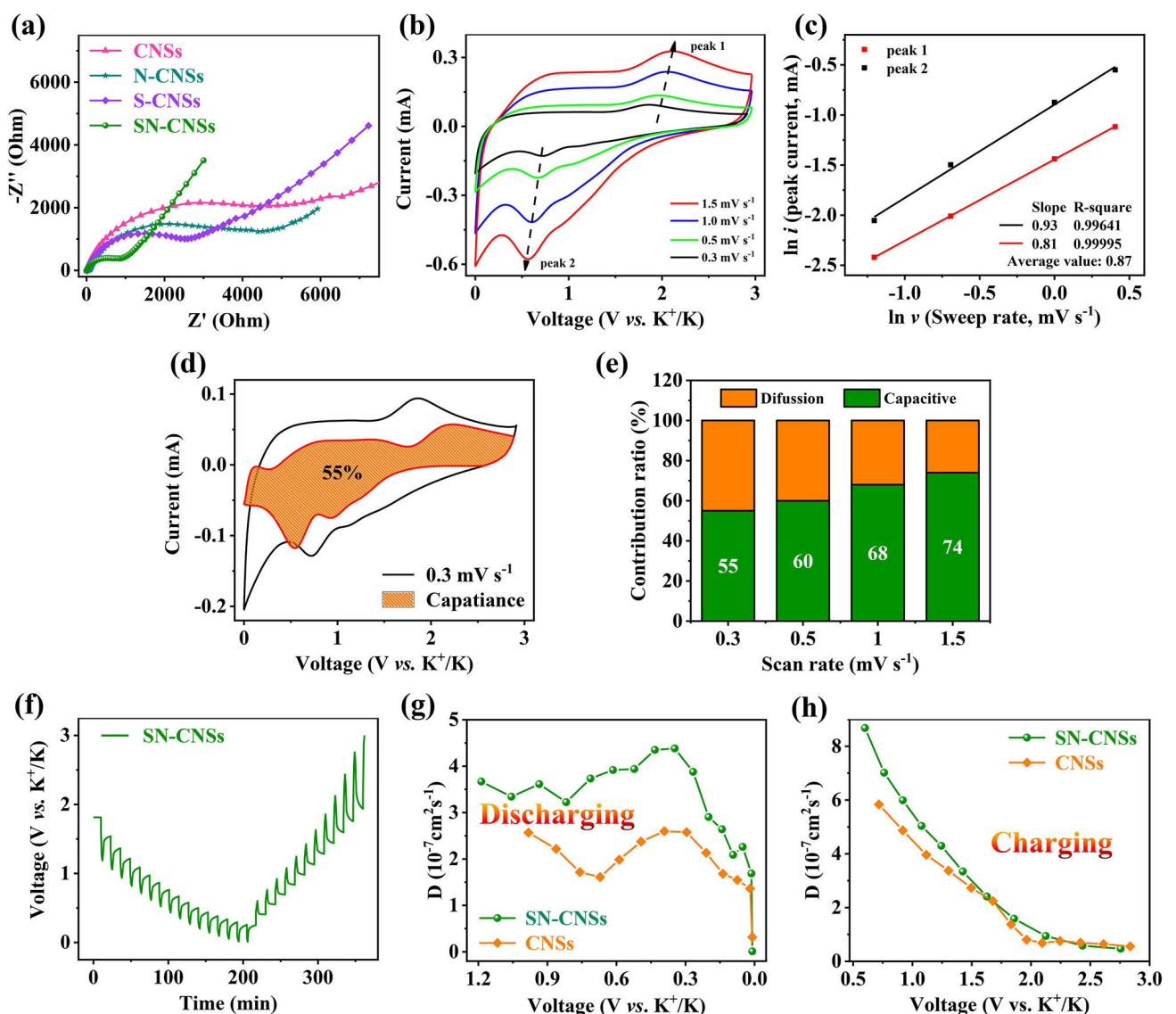


**Figure 4.** Kinetics analysis of SN-CNSs: a) EIS profiles of SN-CNSs and its control samples collected after 500 cycles at  $0.5 \text{ A g}^{-1}$ . b) CV curves under different sweep rates for electrode after 20 charge/discharge cycles at  $500 \text{ mA g}^{-1}$ . c) Line relationship of  $\ln(i)$  versus  $\ln(v)$ . d) Capacitive charge-storage contribution at  $0.3 \text{ mV s}^{-1}$ . e) The ratios of capacitive contribution at different sweep rates. f) Discharge-charge curves of the GITT test for the SN-CNSs electrode. Potassium-ion diffusion coefficient as a function of the state of g) discharging process and h) charging process for the SN-CNSs and CNSs.

gradually decreased, but they did not vanish. It could be attributed to the large specific surface area of the material and the sequence of local reactions caused by the sequential insertion of potassium. At  $0.5 \text{ V}$ , a new intermediate state  $\text{KC}_{24}$  appeared. Finally, XRD diffraction peak at  $33.4^\circ$  suggested the formation of  $\text{KC}_8$  at  $0.01 \text{ V}$ .<sup>[17]</sup> Therefore, the following (de)potassiation reaction could be deduced ( $\text{KC}_{36} \leftrightarrow \text{KC}_{24} \leftrightarrow \text{KC}_8$ ). Interestingly, these peaks between  $27^\circ$ – $33^\circ$  could be indexed to  $\text{K}_3\text{F}_2(\text{PO}_3)$  occurring in almost all states of charge for electrode, which could be attributed to the formation of SEI film. An interfacial transfer behavior of  $\text{KPF}_6$  of electrolyte produced  $\text{K}_3\text{F}_2(\text{PO}_3)$  to construct SEI, where  $\text{K}_3\text{F}_2(\text{PO}_3)$  nanograins not only enhanced the stability of SEI by a stable scaffold but also generated more diffusion paths for  $\text{K}^+$  ions.<sup>[57]</sup> During charging, the phase transition is reversed (Figure 5f). These results of ex-situ measurements robustly suggested a highly

cyclic reversibility of such a S/N co-doped carbon allowing  $\text{K}^+$  to run back and forth through it repeatedly and rapidly.

The adsorption energy on carbon was simulated to investigate adsorption sites and adsorption capacity by DFT. The para-S/N-doped carbon produced a migration barrier energy of  $0.103 \text{ eV}$ , clearly lower than those of  $0.309 \text{ eV}$  for ortho-S/N-doped carbon and  $0.176 \text{ eV}$  for meta-S/N-doped carbon (Figure S17). According to our template synthesis experiment, the fishnet-shaped structure models were constructed and optimized, including the fishnet-shaped curved carbon (Figure 6a), the flat carbon, and S/N-doped defects. Regarding the different covalencies of S and N, it is speculated that the change in hybridization of the carbon with its neighbours (from  $\text{sp}^2$  to  $\text{sp}^2\text{-sp}^3$  hybrid) may also be responsible for the doping-induced polarization in the porous carbon system (Figure 6b).<sup>[58]</sup> At the point of formation energy, the

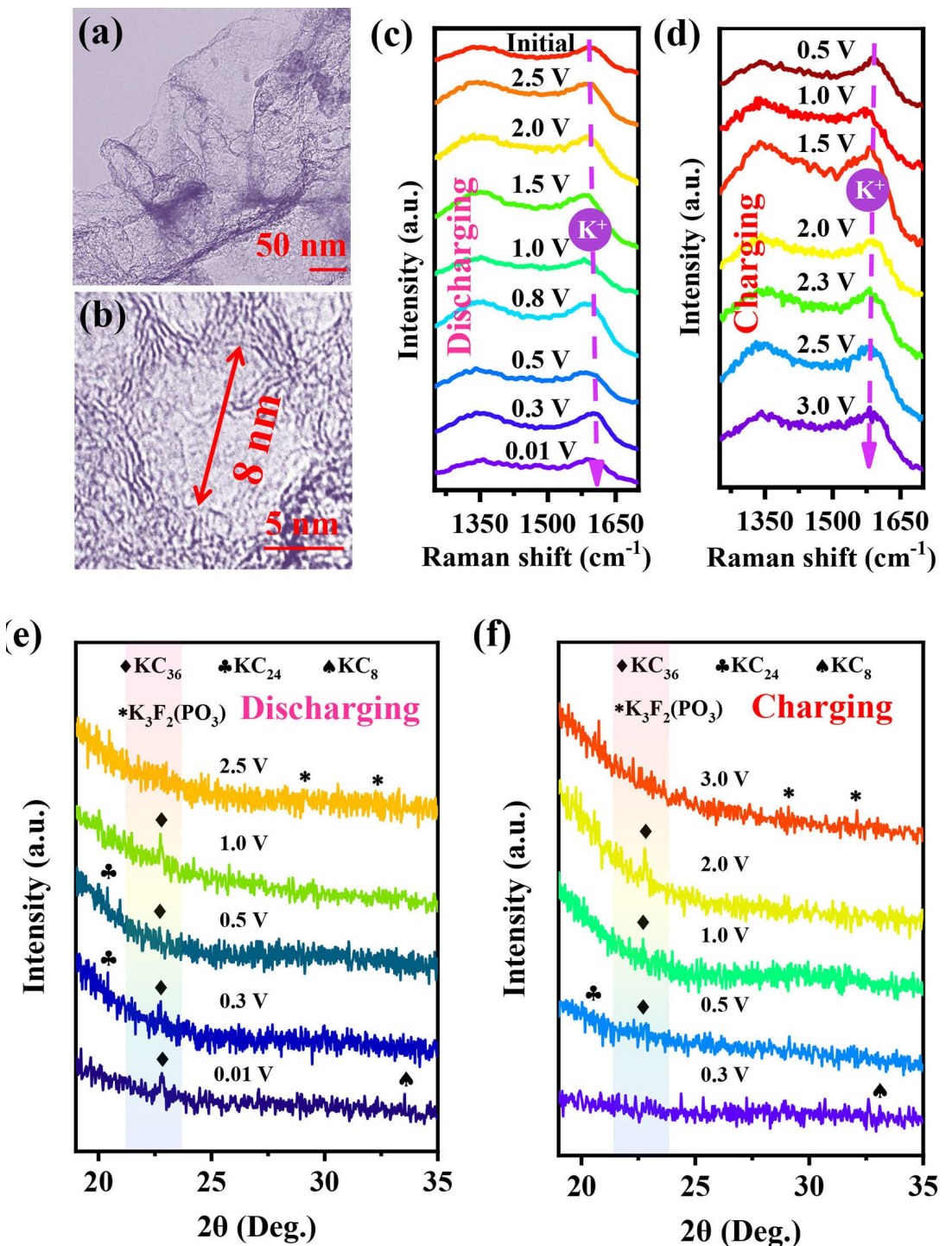


**Figure 5.** a) TEM image, b) HRTEM of SN-CNSs after 1000 cycles at  $1 \text{ A g}^{-1}$ . Ex-situ Raman spectra of SN-CNSs with different states of c) discharging and d) charging. Ex-situ XRD patterns of SN-CNSs with different states of e) discharging and f) charging.

formation energies of pyrrolic nitrogen and S-doped five-membered ring-defected structures were low to 0.201 eV and 0.320 eV, respectively, meaning that it may be energetically beneficial to produce heteroatom doping (Figure S18). Based on the most stable doping structure obtained above, DFT calculations on K-adsorption capabilities ( $\Delta E_{\text{ads}}$ ) of fishnet-shaped curved carbon are performed to gather  $\Delta E_{\text{ads}}$  of

-1.21 eV when potassium atom was ready to close to the hole (Figure 6c). Compared with the flat carbon structure of  $\text{sp}^2$  hybrid, the results showed that the potassium adsorption capacity was -1.05 eV (Figure S19), which was much weaker than the fishnet-like microstructure carbon ( $\text{sp}^2\text{-sp}^3$  hybrid, -1.87 eV), thus confirmed the superiority of the designed structure. Moreover, S/N co-doped had much stronger adsorp-

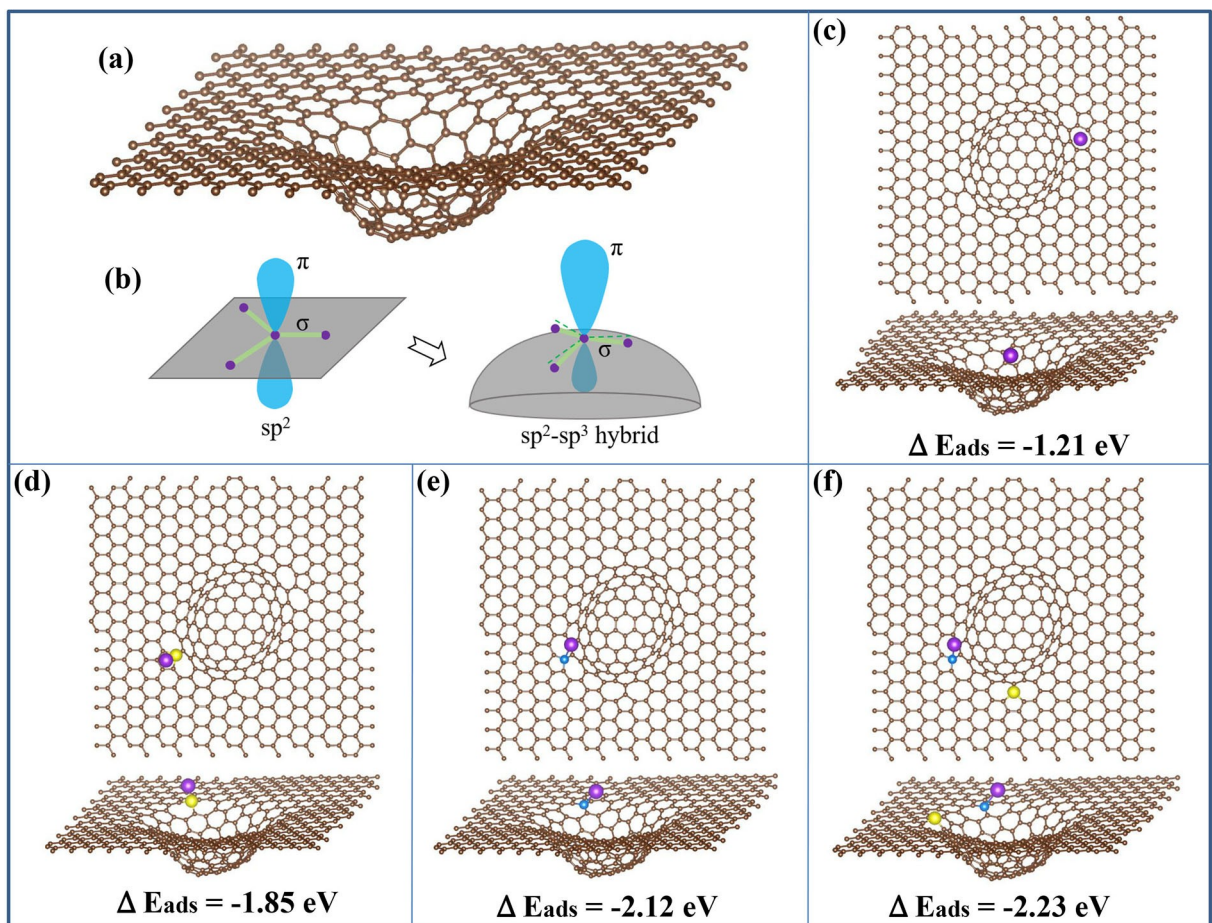


**Figure 6.** a) Crystal model of the fishnet-shaped microstructure carbon system. b) A schematic of electron cloud distortion from the flat carbon to curved carbon leading to polarization. The gray surfaces represent the carbon planes, the purple dots and green bars form the C–C bonds, and the blue spindle shapes stand for the hybrid orbital, respectively. c) A single K atom adsorbed at the edge site of the fishnet-shaped curved carbon. d) K atom adsorbed around the S defect. e) K atom adsorbed around the N defect, and f) K atom adsorbed around the S/N defects. The gray partial double bonds represent the carbon planes, the blue, yellow and purple spheres are the N, S and K atoms, respectively.

tion to  $K^+$  ( $-2.23 \text{ eV}$ ) than N-doped ( $-2.12 \text{ eV}$ ) and S-doped sample ( $-1.85 \text{ eV}$ ) (Figure 6d-f). The  $\Delta E_{ads}$  in defective carbon is much higher than the un-doped carbon, manifesting that the implantation of heteroatoms is energetically advantage at increasing the K-ion storage capacity. Moreover, the S/N co-doping produced a dramatically improved tendency for  $K^+$  attraction as compared with single-atom doping. More importantly, the fishnet-shaped curved carbon maintained a consistent and stable structure permitting ten potassium atoms inserting into it concurrently, dispelling a huge volume expansion which often appeared in graphite even if only one potassium atom was inserted (Figure S19).<sup>[59]</sup> Such a conclusion obtained from DFT calculations have been confirmed by the electrochemical performance test results (Figure 3).

Some interesting remarkable features emerged. (1) Sulfur/nitrogen co-doped in-plane porous carbon nanosheets with fishnet-shaped microstructure have been synthesized via a facile route. (2) The well-designed in-plane porous structure and interconnected carbon flake network enable accelerated diffusion of potassium ions and enhanced kinetics. (3) S/N co-doping could increase the interlayer spacing, produce lots of

defects and edges, and improve the capability of K-ion adsorption. Such a multi-scaled, multi-pored and multi-bonded microstructure has been evidenced by ex-situ TEM, ex-situ Raman and ex-situ XRD. (4) Based on above-mentioned physical-chemical structural features, the models were constructed and optimized for DFT calculations. DFT calculations showed that single transition state and high adsorption energy led to an energetically favorable mechanism for potassium storage for S/N co-doped carbon. Taken together, all characteristic attributes in current materials. i.e., microporous structure including pores and defects, chemical bonding and thermodynamics, are conducive to adsorption and migration of  $K^+$  ions, further leading to such an outstanding electrochemical performance. Such superior results make SN-CNSs electrode a reliable candidate in accomplishing a long-term cycling life.

## Conclusion

A facile and low-cost strategy has been adopted to generate carbon nanosheets with interconnected carbon flake network,

in-plane porous and sulfur/nitrogen co-doping. The combination of multi-scaled templates and low temperature graphitization lead to a multi-scaled and multi-bonded partially graphitized carbon. The unique structure could accelerate the diffusion of potassium ions, alleviate the volume expansion during charge/discharge, and provide sufficient active sites to improve the capacity of K-ion adsorption. Therefore, SN-CNSs delivered a high reversible capacity of  $248 \text{ mAh g}^{-1}$  at a current density of  $1 \text{ A g}^{-1}$  after 4500 cycles. DFT calculations further verified the advantage of S/N co-doping in the adsorption/diffusion of K-ion in SN-CNSs materials. Such excellent performance showed that SN-CNSs possessed a great potential to be a superior anode of potassium-ion batteries.

## Experimental Section

### Materials

All the chemicals and reagents used in the experiment were analytical grade without any further purification. Iron acetylacetone (Aladdin Industrial Co., Shanghai, China), NaCl (Guangzhou Chemical Reagent Factory, Guangdong, China), sulfur powder (Kemiou Chemical Reagent Co., Tianjin, China) and urea (Guangdong Guanghua Sci-Tech Co., Guangdong, China) were commercially available.

### Synthesis of sulfur/nitrogen co-doped in-plane porous carbon nanosheets (SN-CNSs)

Iron acetylacetone and NaCl (mass ratio of 1:2) were mixed with a planetary ball mill for 4 h. Then, sulfur powder and urea were allowed to add into the above sample (mass ratio of 1:1:10) to obtain precursor after grinding for 0.5 h. Subsequently, the uniformly dispersed precursor was carbonized at  $700^\circ\text{C}$  for 5 h under Ar atmosphere with a temperature ramp rate of  $5^\circ\text{C min}^{-1}$ . As-obtained dark product was then washed with  $3 \text{ mol L}^{-1}$  hydrochloric acid through hydrothermal method to remove in-situ generated template (iron) and NaCl. After drying in an oven at  $60^\circ\text{C}$  for 10 h, sulfur/nitrogen co-doped in-plane porous carbon nanosheets were finally collected (abbreviated as SN-CNSs). For comparison, the carbon nanosheets without urea or sulfur additives was prepared by the same procedures, and marked as S-CNSs (no nitrogen) or N-CNSs (no sulfur) or CNSs (no nitrogen/sulfur), respectively.

### Material characterizations

Powder X-ray diffraction (XRD) was taken to examine the crystal structure and phase composition with Cu  $K_\alpha$  source operated at 40 kV and 40 mA in the  $2\theta$  range from  $10^\circ$  to  $80^\circ$  (D8 Advance, Bruker, Germany). The element valence and chemically-bonded states in particles were characterized by the X-ray photoelectron spectroscopy (XPS) (Kratos Axis Ultra DLD, Japan) using a standard Al  $K_\alpha$  source (1486.6 eV). Raman spectra (LabRAM Aramis, HJY, France) and Fourier transform infrared spectrometers (FT-IR) (Bruker Tensor 27, Germany) were utilized to deeply understand the molecular-scaled structural characteristic of carbon. Nitrogen adsorption-desorption isotherms were acquired on a Brunauer-Emmett-Teller (BET) instrument to analyze specific surface area and pore size (3H-2000PS1, BeiShiDe Co., Beijing, China).  $\text{CO}_2$  adsorption-desorption isotherms were acquired on a Brunauer-Emmett-Teller (BET) instrument to analyze specific surface area and pore

size (Micromeritics, ASAP 2020 V4.03). The morphology and microstructure of obtained samples were carefully observed by scanning electron microscope (SEM) (Zeiss Ultra 55, Germany) and Transmission electron microscopy (TEM) (JEM-2100HR, Tokyo, Japan), high-resolution TEM (HRTEM), STEM and energy dispersive X-ray spectroscope (EDX, Oxford instrument).

### Electrochemical measurements

The active material, CMC, SBR, and acetylene black (Super P) (mass ratio of 8:0.5:0.5:1) were dispersed in deionized water to form homogenous slurries, subsequently covered on Cu foil to collect work electrode after drying, punching and calendaring, with a mass loading of  $0.8\text{--}1.0 \text{ mg cm}^{-2}$ . The coin cells were ultimately assembled in an argon-filled glovebox (Etelux, Lab2000, Beijing, China). Potassium foil was utilized as counter electrode, and  $1 \text{ M } \text{KPF}_6$  in a mixed solvent, consisting of ethylene carbonate, diethyl carbonate by 1:1 in volume, was served as electrolyte. Glass fiber was used as separator. Electrochemical cyclic performances were measured by a battery test system (Neware, BTS2300, Shenzhen, China) under a voltage range from 0.01 to  $3.0 \text{ V}$  in a constant-temperature incubator (Fengleng, SPX-250, Shanghai, China) (ambient temperature). The cyclic voltammetry (CV) curves and the data of electrochemical impedance spectroscope (EIS) (0.01 Hz–100 kHz) were collected by an electrochemical work station (CHI600E, Shanghai, China).

### DFT calculations

Density functional theory (DFT) calculations are performed by using the projector augmented wave (PAW) method, as implemented in the Vienna *ab initio* simulation package (VASP).<sup>[60,61]</sup> The exchange-correlation functional is presented by the generalized gradient approximation (GGA) with the parametrization scheme of Perdew, Burke, and Ernzerhof (PBE).<sup>[62,63]</sup> The plane-wave basis set with a cutoff energy of 500 eV is used. A  $8 \times 14$  rectangle supercell of the combined graphene system is employed to model the fishnet-shaped microstructure, dopant defects and the potassium adsorption. The flat carbon layer with nanopore is put in the  $xy$  plane, the in-plane lattice constant of supercell is  $34.2 \times 34.6 \text{ \AA}^2$ . Half of  $\text{C}_{240}$  molecule is deposited on the nanopore forming the fishnet-shaped microstructure system, and a vacuum layer of  $30 \text{ \AA}$  is used in the  $z$  direction to eliminate the interaction between its periodic replicas. The Brillouin zone (BZ) integration is approximated by using a special  $k$ -point sampling of the Monkhorst-Pack scheme with a  $\Gamma$ -centered grid. In the structural relaxation and the property calculation, a  $3 \times 3 \times 1$   $k$ -grid is adopted.<sup>[64]</sup> In the geometry optimization, all atoms are allowed to relax until forces on atoms are less than  $0.02 \text{ eV \AA}^{-1}$ . In the present study, we consider three typical point dopants in the porous carbon, that is, nitrogen doping, sulfur doping and nitrogen/sulfur co-doping defects. The formation energy ( $E_f$ ) of substitution defect was calculated for comparing the relative stability of the doped porous carbon systems by Equation (2):

$$\Delta E_f = E_{\text{tot}}^{\text{doped}} - E_{\text{tot}}^{\text{undoped}} + \sum_i n_i \mu_i \quad (2)$$

where,  $E_{\text{tot}}^{\text{doped}}$  was the total energy of the supercell containing impurities,  $E_{\text{tot}}^{\text{undoped}}$  was the total energy of the supercell without defects,  $n_i$  represented the number of constituent element  $i$  being added/removed from the porous carbon supercell, and  $\mu_i$  referred to the atomic chemical potential.

The adsorption energies of K atoms on the porous carbon systems could be evaluated by the surficial binding energies, which was defined in Equation (3) as

$$\Delta E_{\text{ads}} = E_{\text{porous carbon+K}} - E_{\text{porous carbon}} - E_K \quad (3)$$

where  $E_{\text{porous carbon+K}}$  was the total energy for K atoms adsorbed on the porous carbon supercell,  $E_{\text{porous carbon}}$  was the total energy for the porous carbon system without atomic adsorption, and  $E_K$  was the total energy of a separated molecule as determined from DFT calculations.

## Acknowledgements

This work is supported by National Natural Science Foundation of China (Grant No. 51873074). Science and Technology Bureau of Huangpu District (Research and industrialization of key technologies for high-safety and high-energy density lithium-ion battery materials).

## Conflict of Interest

The authors declare no conflict of interest.

## Data Availability Statement

The data that support the findings of this study are available in the supplementary material of this article.

**Keywords:** carbon nanosheets • DFT calculations • low temperature graphitization • porous structure • potassium-ion batteries anode

- [1] K. Lei, C. Wang, L. Liu, Y. Luo, C. Mu, F. Li, J. Chen, *Angew. Chem. Int. Ed.* **2018**, *130*, 4777–4781.
- [2] Y. Wang, R. Chen, T. Chen, H. Lv, G. Zhu, L. Ma, C. Wang, Z. Jin, J. Liu, *Energy Storage Mater.* **2016**, *4*, 103–129.
- [3] X. Wu, Y. Chen, Z. Xing, C. W. K. Lam, S. S. Pang, W. Zhang, Z. Ju, *Adv. Energy Mater.* **2019**, *9*, 1900343.
- [4] J. Zheng, Y. Yang, X. Fan, G. Ji, X. Ji, H. Wang, S. Hou, M. R. Zachariah, C. Wang, *Energy Environ. Sci.* **2019**, *12*, 615–623.
- [5] W. Zhang, Y. Liu, Z. Guo, *Sci. Adv.* **2019**, *5*, eaav7412.
- [6] C. Lin, Y. Wang, F. Zhong, H. Yu, Y. Yan, S. Wu, *Chem. Eng. J.* **2021**, *407*, 126991.
- [7] F. Zhong, Y. Wang, G. Li, C. Huang, A. Xu, C. Lin, Z. Xu, Y. Yan, S. Wu, *Renewable Sustainable Energy Rev.* **2021**, *146*, 111161.
- [8] Q. Zhang, J. Mao, W. K. Pang, T. Zheng, V. Sencadas, Y. Chen, Y. Liu, Z. Guo, *Adv. Energy Mater.* **2018**, *8*, 1703288.
- [9] P. Xiong, J. Wu, M. Zhou, Y. Xu, *ACS Nano* **2019**, *14*, 1018–1026.
- [10] Y. Wu, H. B. Huang, Y. Feng, Z. S. Wu, Y. Yu, *Adv. Mater.* **2019**, *31*, 1901414.
- [11] Q. Peng, S. Zhang, H. Yang, B. Sheng, R. Xu, Q. Wang, Y. Yu, *ACS Nano* **2020**, *14*, 6024–6033.
- [12] M. Ma, S. Zhang, Y. Yao, H. Wang, H. Huang, R. Xu, J. Wang, X. Zhou, W. Yang, Z. Peng, *Adv. Mater.* **2020**, *32*, 2000958.
- [13] L. Yang, W. Hong, Y. Zhang, Y. Tian, X. Gao, Y. Zhu, G. Zou, H. Hou, X. Ji, *Adv. Funct. Mater.* **2019**, *29*, 1903454.
- [14] Y. Liu, Z. Sun, X. Sun, Y. Lin, K. Tan, J. Sun, L. Liang, L. Hou, C. Yuan, *Angew. Chem. Int. Ed.* **2020**, *59*, 2473–2482; *Angew. Chem.* **2020**, *132*, 2494–2503.
- [15] W. Tian, H. Zhang, X. Duan, H. Sun, G. Shao, S. Wang, *Adv. Funct. Mater.* **2020**, *30*, 1909265.
- [16] Z. Jian, S. Hwang, Z. Li, A. S. Hernandez, X. Wang, Z. Xing, D. Su, X. Ji, *Adv. Funct. Mater.* **2017**, *27*, 1700324.
- [17] Z. Jian, W. Luo, X. Ji, *J. Am. Chem. Soc.* **2015**, *137*, 11566–11569.
- [18] H. Huang, R. Xu, Y. Feng, S. Zeng, Y. Jiang, H. Wang, W. Luo, Y. Yu, *Adv. Mater.* **2020**, *32*, 1904320.
- [19] S. Zhang, Z. Xu, H. Duan, A. Xu, Q. Xia, Y. Yan, S. Wu, *Electrochim. Acta* **2020**, *337*, 135767.
- [20] M. Chen, W. Wang, X. Liang, S. Gong, J. Liu, Q. Wang, S. Guo, H. Yang, *Adv. Energy Mater.* **2018**, *8*, 1800171.
- [21] J. Zhang, C. Yang, Y. Yin, L. Wan, Y. Guo, *Adv. Mater.* **2016**, *28*, 9539–9544.
- [22] C. Zhu, Y. Wen, P. A. van Aken, J. Maier, Y. Yu, *Adv. Funct. Mater.* **2015**, *25*, 2335–2342.
- [23] Y. Cao, L. Xiao, M. L. Sushko, W. Wang, B. Schwenzer, J. Xiao, Z. Nie, L. V. Saraf, Z. Yang, J. Liu, *Nano Lett.* **2012**, *12*, 3783–3787.
- [24] J. Xu, M. Wang, N. P. Wickramaratne, M. Jaroniec, S. Dou, L. Dai, *Adv. Mater.* **2015**, *27*, 2042–2048.
- [25] J. R. Matos, L. P. Mercuri, M. Kruk, M. Jaroniec, *Langmuir* **2002**, *18*, 884–890.
- [26] Y. Zhang, Z. Wang, D. Li, Q. Sun, K. Lai, K. Li, Q. Yuan, X. Liu, L. Ci, *J. Mater. Chem. A* **2020**, *8*, 22874–22885.
- [27] S. Gao, H. Liu, K. Geng, X. Wei, *Nano Energy* **2015**, *12*, 785–793.
- [28] S. Yumitorii, *J. Mater. Sci.* **2000**, *35*, 139–146.
- [29] S. Wang, L. Xia, L. Yu, L. Zhang, H. Wang, X. W. D. Lou, *Adv. Energy Mater.* **2016**, *6*, 1502217.
- [30] X. Wang, Q. Weng, X. Liu, X. Wang, D.-M. Tang, W. Tian, C. Zhang, W. Yi, D. Liu, Y. Bando, D. Golberg, *Nano Lett.* **2014**, *14*, 1164–1171.
- [31] Y. Zuo, P. Li, R. Zang, S. Wang, Z. Man, P. Li, S. Wang, W. Zhou, *ACS Appl. Energ. Mater.* **2021**, *4*, 2282–2291.
- [32] X. Zhao, P. Xiong, J. Meng, Y. Liang, J. Wang, Y. Xu, *J. Mater. Chem. A* **2017**, *5*, 19237–19244.
- [33] W. Li, M. Zhou, H. Li, K. Wang, S. Cheng, K. Jiang, *Energy Environ. Sci.* **2015**, *8*, 2916–2921.
- [34] P. Xiong, X. Han, X. Zhao, P. Bai, Y. Liu, J. Sun, Y. Xu, *ACS Nano* **2019**, *13*, 2536–2543.
- [35] J. Wu, X. Zhang, Z. Li, C. Yang, W. Zhong, W. Li, C. Zhang, N. Yang, Q. Zhang, X. Li, *Adv. Funct. Mater.* **2020**, *30*, 2004348.
- [36] X. Wu, Z. Xing, Y. Hu, Y. Zhang, Y. Sun, Z. Ju, J. Liu, Q. Zhuang, *Ionics* **2019**, *25*, 2563–2574.
- [37] C. Liu, N. Xiao, H. Li, Q. Dong, Y. Wang, H. Li, S. Wang, X. Zhang, J. Qiu, *Chem. Eng. J.* **2019**, *382*, 121759.
- [38] J. Li, Y. Li, X. Ma, K. Zhang, J. Hu, C. Yang, M. Liu, *Chem. Eng. J.* **2019**, *384*, 123328.
- [39] Y. Liu, H. Dai, L. Wu, W. Zhou, L. He, W. Wang, W. Yan, Q. Huang, L. Fu, Y. Wu, *Adv. Energy Mater.* **2019**, *9*, 1901379.
- [40] C. Lu, Z. Sun, L. Yu, X. Lian, Y. Yi, J. Li, Z. Liu, S. Dou, J. Sun, *Adv. Energy Mater.* **2020**, *10*, 2001161.
- [41] M. Chen, Y. Cao, C. Ma, H. Yang, *Nano Energy* **2020**, *81*, 105640.
- [42] X. Shi, Y. Zhang, G. Xu, S. Guo, A. Pan, J. Zhou, S. Liang, *Sci. Bull.* **2020**, *65*, 2014–2021.
- [43] X. Li, M. Chen, L. Wang, H. Xu, J. Zhong, M. Zhang, Y. Wang, Q. Zhang, L. Mei, T. Wang, J. Zhu, B. Lu, X. Duan, *Nanoscale Horiz.* **2020**, *5*, 1586–1595.
- [44] Y. Zhang, S. Tian, C. Yang, J. Nan, *Dalton Trans.* **2020**, *49*, 5108–5120.
- [45] Z. Qiu, K. Zhao, J. Liu, S. Xia, *Electrochim. Acta* **2020**, *340*, 135947.
- [46] Y. Zhang, L. Li, Y. Xiang, G. Zou, H. Hou, W. Deng, X. Ji, *ACS Appl. Mater. Interfaces* **2020**, *12*, 30431–30437.
- [47] Y. Liu, H. Dai, Y. An, L. Fu, Q. An, Y. Wu, *J. Mater. Chem. A* **2020**, *8*, 14993–15001.
- [48] Y. Sun, H. Wang, W. Wei, Y. Zheng, L. Tao, Y. Wang, M. Huang, J. Shi, Z. Shi, D. Mitlin, *ACS Nano* **2021**, *15*, 1652–1665.
- [49] L. Tao, Y. Yang, H. Wang, Y. Zheng, H. Hao, W. Song, J. Shi, M. Huang, D. Mitlin, *Energy Storage Mater.* **2020**, *27*, 212–225.
- [50] W. Wei, Y. Zheng, M. Huang, J. Shi, L. Li, Z. Shi, S. Liu, H. Wang, *Nanoscale* **2021**, *13*, 4911–4920.
- [51] W. Zhang, H. Wang, R. Liao, W. Wei, X. Li, S. Liu, M. Huang, Z. Shi, J. Shi, *New Carbon. Mater.* **2021**, *36*, 167–178.
- [52] J. Chen, Y. Cheng, Q. Zhang, C. Luo, H. Li, Y. Wu, H. Zhang, X. Wang, H. Liu, X. He, J. Han, D. Peng, M. Liu, M. Wang, *Adv. Funct. Mater.* **2021**, *31*, 2007158.
- [53] T. Brezesinski, J. Wang, S. H. Tolbert, B. Dunn, *Nat. Mater.* **2010**, *9*, 146–151.

- [54] V. Augustyn, J. Come, M. A. Lowe, J. W. Kim, P. L. Taberna, S. H. Tolbert, H. D. Abruna, P. Simon, B. Dunn, *Nat. Mater.* **2013**, *12*, 518–522.
- [55] C. Huang, A. Xu, G. Li, H. Sun, S. Wu, Z. Xu, Y. Yan, *Small* **2021**, *17*, 2100685.
- [56] K. Share, A. P. Cohn, R. Carter, B. Rogers, C. L. Pint, *ACS Nano* **2016**, *10*, 9738–9744.
- [57] W. Feng, Y. Cui, W. Liu, H. Wang, Y. Zhang, Y. Du, S. Liu, H. Wang, X. Gao, T. Wang, *ACS Nano* **2020**, *14*, 4938–4949.
- [58] M. Kothari, M. H. Cha, K. S. Kim, *Proc. Roy. Soc. A* **2018**, *474*, 20180054.
- [59] Y. Qian, S. Jiang, Y. Li, Z. Yi, J. Zhou, J. Tian, N. Lin, Y. Qian, *Energy Storage Mater.* **2020**, *29*, 341–349.
- [60] G. Kresse, J. Furthmüller, *Comput. Mater. Sci.* **1996**, *6*, 15–50.
- [61] G. Kresse, J. Furthmüller, *Phys. Rev. B* **1996**, *54*, 11169.
- [62] J. P. Perdew, K. Burke, M. Ernzerhof, *Phys. Rev. Lett.* **1996**, *77*, 3865–3868.
- [63] G. Kresse, D. Joubert, *Phys. Rev. B* **1999**, *59*, 1758–1775.
- [64] H. J. Monkhorst, J. D. Pack, *Phys. Rev. B* **1976**, *13*, 5188–5192.

Manuscript received: December 6, 2021  
Revised manuscript received: January 15, 2022  
Accepted manuscript online: January 19, 2022  
Version of record online: February 9, 2022